Journal of
Materials Chemistry A

ROYAL SOCIETY
OF CHEMISTRY

PAPER

View Article Online
View Journal | View Issue

Check for updates

Cite this: *J. Mater. Chem. A*, 2024, **12**, 4312

Probing host–dopant interactions in conducting polymers for improved performance of electrochemical deionization†

Hung-Yi Huang, Yi-Heng Tu, Yu-Hsiang Yang, Yi-An Chen, Wei-Lin Lee, Meng-Fei Wu, Ho-Hsiu Chou and Chi-Chang Hu *

Received 13th November 2023
Accepted 8th January 2024

DOI: 10.1039/d3ta06973g

rsc.li/materials-a

The escalating global scarcity of water resources has amplified the need to develop efficient desalination methods. Electrochemical deionization (ECDI) has emerged as a promising method to solve this pressing issue. Among various ECDI systems, conducting polymers have showcased remarkable potential for electrode materials due to their facile large-scale synthesis and precise control over the removal of anions and cations. We scrutinized the impact of diverse dopant sizes on the intrinsic properties of polypyrrole (PPy) chains, leading to the development of a high-performance ECDI system. Incorporation of *para*-substituted groups featuring elongated carbon chains, such as dodecylbenzene sulfonate (DBS), the PPy-DBS-1//PPy-ClO_4 configuration attained a salt-adsorption capacity (SAC) of 61.7 mg g^{-1} in NaCl solution (10 mM) and sustained low energy consumption (0.22 kW h/kg-NaCl). Our findings suggest that the size and type of dopant have key roles in enhancing the ion transport and mobility of charge carriers within the conducting-polymer framework. Moreover, fine-tuning the doping ratio enhanced the cation-capture ability of electrodes and sustained their cycling stability. Overall, these insights into the symbiotic relationship between dopants and PPy framework within an ECDI system provide guidance framework for augmenting the electrode performance of conducting polymers with dopants, and expanding the potential applications of conducting polymers in ECDI.

1. Introduction

In response to population growth, obtaining clean water through energy-saving and environmentally friendly methods has become a pressing concern globally. With seawater accounting for 97% of water on the planet, seawater desalination is a common method for producing clean water.[1] However, traditional methods of seawater desalination, such as thermal or membrane treatments, have several drawbacks, including high energy consumption and secondary pollution. In recent years, researchers have been exploring alternative techniques. Electrochemical deionization (ECDI) is of particular interest due to its ease of operation and lack of heat-treatment requirements.[2] The conventional method of an ECDI system relies predominantly on the properties of electric double-layer (EDL) materials to remove salts by applying an external electric field to induce the electrodes to adsorb ions of opposite charge.[3,4] However, the practical value of this conventional method is limited by the EDL mechanism, which restricts the desalination capability.[5]

Utilization of pseudocapacitive-type or battery-type faradaic materials has emerged as a prominent research area in the field of ECDI for addressing the drawbacks of conventional EDL-type materials.[6] This approach involves the capture of anions and cations in a solution through charge transfer within electrodes, which effectively reduces energy consumption and enhances the desalination performance. In addition, the unique "memory effect" of faradaic materials proposed by Hu *et al.* enables resource recovery and water purification simultaneously without the need for membranes, which has further boosted the appeal of such materials.[7] The development of faradaic materials for applications in ECDI is underway with great enthusiasm. Among these materials, metal oxides have been used extensively for cation trapping[8] because of their large theoretical capacity and superior stability.[9,10] However, their application in anion trapping is limited by their material properties.[11] In contrast, the intrinsic properties of polymers are susceptible to the influence of small molecules.[12] For instance, conducting polymers can generate electrons or polarons on the polymer skeleton through doped ionophores, which creates exceptional possibilities for utilization in ECDI.[13,14] In the pursuit of improving the performance of conducting polymers in ECDI systems, the incorporation of composites[15–17] and appropriate

---

*Department of Chemical Engineering, National Tsing Hua University, 101, Section 2, Kuang-Fu Road, Hsin-Chu, 300044, Taiwan. E-mail: cchu@che.nthu.edu.tw; Web: **https://mx.nthu.edu.tw/~cchu/**; Fax: +886-3-5736027; Tel: +886-3-5736027*

† Electronic supplementary information (ESI) available. See DOI: **https://doi.org/10.1039/d3ta06973g**

doping ions[18] are the most used methods among this field. Previously, we demonstrated the potential of polypyrrole (PPy)-based electrodes incorporated with dopants in different sizes for achieving a low cell-voltage (0.75 V/−0.2 V) ECDI system. It was observed that large dopants, such as 4-methylbenzenesulfonic acid (p-TS), were effective in cation-capturing, whereas small dopants such as perchlorate (ClO_4) could move freely to facilitate the anion-exchange capability of the PPy-ClO_4 electrode.[19] That study laid the groundwork for a follow-up study of the interaction between PPy and doped ions in ECDI systems.

However, the strategy for selecting appropriate dopants in PPy-based ECDI systems for cation-removal remains a mystery. Researchers have extensively explored the impact of doping different types of ions in conducting polymers, such as PPy, on their intrinsic properties.[20,21] For instance, Bay *et al.* investigated the properties of PPy doped with various alkyl benzenesulfonates (ABSA) using the electrochemical quartz crystal microbalance (EQCM). They observed that the doping efficiency improved with an extension of the carbon-chain length of doped ions. In addition, anion movement was visible on small doping anions (shorter carbon chains) through the dimensional change, whereas large doping anions did not show such movement.[22] Conversely, Rhee *et al.* used small-angle X-ray diffraction to demonstrate that ABSA with long carbon chains could act as a spacer between PPy chains and induce lamellar structures during PPy synthesis.[23] Nevertheless, even though studies have observed that dopant–host interactions affect the intrinsic properties of conducting polymers significantly, a comprehensive investigation of how such interactions can enhance the capability of conducting polymers for deionization applications is lacking.

Therefore, the main objective of this study was to examine the influence of varying dopant sizes on the intrinsic properties of PPy chains, and craft a high-performance ECDI system by selecting the appropriate dopant. Initially, the study focused on the effects of altering *para*-substituted functional groups in benzenesulfonate on doping efficiency, thereby potentially enhancing cation-capturing sites. Furthermore, with the same actual doping ratio, we analyzed the material characteristics and performance of PPy in capturing cations when different dopants were employed. In this way, we elucidated the deionization mechanism induced by different dopants within polymer frameworks. Ultimately, we identified the most suitable dopant-induced conducting-polymer structure and fine-tuned the desalination performance of the PPy-based ECDI system by adjusting the suitable doping ratio within electrode materials.

2. Experimental and methods

The details of purchased chemicals, synthesis system, characterization methods, and electrochemical measurements of PPy-doped materials are presented in Section 1 in the ESI.†

2.1. Pretreatments of titanium substrates

A commercial titanium sheet underwent acid etching in 6 M hydrochloric acid at 70 °C for 30 min to remove the native oxide or contaminants. Next, the "pickled" titanium sheet was immersed in RuO_2 solution (0.3 mg mL^{-1} in DI water) and dried in an oven at 80 °C thrice. The pretreated titanium sheets were annealed at 250 °C for 2 h, resulting in a thin layer of RuO_2 forming on the substrate. The RuO_2 layer simultaneously acted as a protective layer against substrate oxidation and improved the coating uniformity of PPy (which provides no ion-removal capacity).

2.2. Synthesis of PPy electrodes with various dopants

PPy-coated electrodes were prepared *via* electrochemical polymerization using a three-electrode system with a fixed area of the working electrode of 1 cm × 3 cm. The coating electrolyte was an aqueous solution containing 0.1 M pyrrole monomer and 0.05 M dopant (*i.e.*, sulfur/nitrogen (S/N) molar ratio of 0.5). A galvanostatic mode was employed to deposit PPy thin films onto the surface of a RuO_2-coated titanium sheet, and the operation parameters are shown in the ESI.† This method ensured precise control over the doping process, thereby yielding reproducible and high-quality PPy-coated electrodes.

In a previous study,[19] we found that the dopant size influenced the anion- or cation-exchange ability of PPy. Accordingly, $LiClO_4$ was chosen as the negative-electrode dopant salt for the PPy-ClO_4 electrode. To investigate the impact of dopants on the cation-exchange ability of PPy, we chose sodium dodecylbenzene sulfonate (DBS), sodium styrene 4-sulfonate (SS), and sodium 4-hydroxybenzene sulfonate (HBS) as the dopant salts with a S/N molar ratio of 0.5 to fabricate PPy-DBS-1, PPy-SS-1, and PPy-HBS-1, respectively, as positive electrodes in the ECDI system. To eliminate the effect of the actual doping ratios, the same synthetic procedure was adopted to prepare PPy-DBS-1, PPy-SS-2, and PPy-HBS-2 with the same actual S/N ratio of 0.45 by controlling the concentration of doping salts in the coating electrolytes based on elemental analysis.

2.3. Tests of desalination performance

Desalination experiments were conducted using a flow-by ECDI cell consisting of a monitoring section and experimental section (Fig. S1†). The ECDI cell comprised PPy electrodes doped with benzenesulfonate analogues and ClO_4^- as positive and negative electrodes, respectively. The desalination test was conducted using a 75 mL, sodium chloride solution (10 mM) with a feed flow rate of 30 mL min^{-1} into the ECDI cell.

To establish the relationship between the maximum operating potential window and salt-adsorption capacity (SAC), the programming method for cell voltage was applied.[24] Also, the ratio of the charging time/discharging time on positive and negative electrodes was balanced through the salt-adsorption rate (SAR). In addition, by adjusting the thickness of the active material and the solution concentration, the desalination capacity of the ECDI system was enhanced, thereby effectively improving the ion-diffusion rate. The calibration curve between the NaCl concentration and conductivity, as well as the calculation methods for SAC (mg g^{-1}), SAR (mg g^{-1} min^{-1}), energy consumption (EC; kW h/kg-NaCl), and retention of SAC (R_{SAC}), can be found in the ESI.†

3. Results and discussion

3.1. Morphologic and structural characterizations of PPy-based electrodes

3.1.1. PPy electrodes with different dopants at the same molar ratio. The composition of various PPy electrodes was determined using elemental analysis (Table S1†). Notably, the S/N molar ratio of the PPy-DBS-1 electrode (0.45) was considerably higher than those of PPy-SS-1 and PPy-HBS-1 electrodes, suggesting that the size of dopants has a critical role in determining the doping efficiency.[22] During electropolymerization, the lipophilic and hydrophilic sides of DBS facilitated uniform doping in the PPy chain, resulting in the highest doping efficiency within the PPy-DBS-1 electrode.[25] However, the doping efficiency of PPy-SS-1 decreased with the scaling down of doped molecules but was retained at a certain level (0.33). Conversely, the absence of a lipophilic moiety with long carbon chains in HBS rendered a challenge to doping in the PPy-HBS-1 electrode. To visualize the impact of dopants on the doping efficiency, linear sweep voltammetry (LSV) curves were constructed during the electropolymerization of the PPy electrode (Fig. S2†). DBS could promote the uniform dispersion of monomers in an aqueous solution, probably acting as a surfactant and resulting in the lowest onset potential of electropolymerization and highest doping efficiency.

After confirming the doping efficiency of PPy electrodes, we undertook the material analysis of PPy-based electrodes containing various large dopants (Fig. 1). The PPy-DBS-1 electrode displayed a significantly reduced contact angle of only 9.99° after resting for 60 s (Fig. 1a), thereby reflecting that the excellent doping efficiency enabled the electrode to contain the most hydrophilic functional groups. With the shortening and substitution of carbon chains in dopants, PPy-SS-1 and PPy-HBS-1 electrodes exhibited higher contact angles (Fig. 1b and c). In contrast, the PPy-HBS-1 electrode showed the largest contact angle in initial and final states due to its lowest dopant efficiency, thereby highlighting the significant effect of doped ions on electrode hydrophilicity.

Scanning electron microscopy (SEM) was also utilized to observe the variation in morphology of PPy-coated electrodes with changes in dopants (Fig. S3†). Under low-magnification SEM (Fig. S3a–c†), use of PPy-SS-1 and PPy-HBS-1 electrodes led to the formation of a typical "cauliflower-like" morphology in PPy aggregates. In contrast, the PPy-DBS-1 electrode exhibited a markedly different morphology, close to a block-like structure. This distinct morphologic characteristic could be attributed to the effects of steric hindrance of the long carbon chains present in DBS molecules, as discussed previously.[21,23] High-magnification SEM (Fig. S3d–f†) revealed the cauliflower-like morphology of PPy-SS-1 and PPy-HBS-1 electrodes to be composed of spherically aggregated PPy particles. The PPy-DBS-1 electrode, on the other hand, displayed a bulk structure due to the incorporation of large anionic dopants. Comparison of cross-section images in Fig. S3g–i† revealed that the DBS dopant could induce a relaxed PPy aggregate structure due to its larger molecular structure.[26]

To further elucidate the impact of the dopant on the agglomeration structure of PPy, XRD analysis was employed to characterize the microstructure of PPy electrodes. As depicted in Fig. 1d, none of the PPy electrodes exhibited distinct, sharp peaks, but instead broad asymmetric scattering peaks extending from 15 to 30°. Except for the PPy-DBS-1 electrode, the other two PPy electrodes displayed a broad peak around $2\theta = 26°$, corresponding to a d-spacing of 3.427 Å, revealing the amorphous structure and short-range orderly arrangement of the PPy chain.[27] Nevertheless, the broad peak in the PPy-DBS-1 electrode comprised two independent peaks at approximately $2\theta = 18°$ and 26°, with the former peak being attributed to the scattering of the pyrrole-counter ion or inter-counter ion interaction.[23,28] Moreover, the smaller 2θ value corresponded to a larger d-spacing (4.92 Å), which supported the notion that DBS doping leads to a more relaxed agglomerative structure resulting from interactions among the PPy chain, thereby enhancing utilization of active sites within the PPy.[18]

Cyclic voltammetry (CV) (Fig. S4†) was essential for assessing the impact of host–dopant interactions on the anion/cation-exchange properties of PPy-doped electrodes at the same S/N molar ratio. Except for the PPy-DBS-1 electrode, the other dopants induced two redox pairs in CV curves. According to the literature employing the EQCM,[29] these redox pairs corresponded to cation exchange and anion exchange, respectively. However, with the incorporation of large anionic dopants, such as DBS, only a single redox pair was observed at negative potentials. This phenomenon is attributable to the large anion dopants which impede anion exchange within the PPy film, thus predisposing the PPy-DBS-1 electrode towards cation-exchange predominance and enhancing its cation-capture capability. Furthermore, the PPy-HBS-1 electrode exhibited the highest reduction peak current. This observation was presumably due to the small size of HBS ions, which are more likely to participate in anion exchange, thereby resulting in cumulative response currents from anion and cation exchanges at negative potentials.

Raman spectroscopy (Fig. 1e and Table S2†) was used to gain further insights into host–dopant interactions.[30] This analysis is particularly effective due to the sensitivity of the Raman spectrum to the local structural defects associated with the polymer chain, which are typically attributed to the protonated polarons and bipolaron of PPy.[31] The peaks at 1084 and 1377 cm^{-1} appeared only on the PPy-DBS-1 electrode, which was attributed to the bending vibration of polarons. Additionally, X-ray photoelectron spectroscopy (XPS) at the N 1s core level was used to provide more accurate evidence for the significant effects of dopants and doping efficiencies on the protonation state of the PPy backbone (refer to Fig. 1f and Table S3†). The intense peak between 399.3 and 399.5 eV was assigned to the neutral nitrogen in the pyrrole ring (–N–H bond),[13] whereas a peak shifted to a higher binding energy (around 401–401.3 eV) was attributed to positively charged nitrogen (–N–H$^+$ bond) in the polaron.[32] Moreover, the peak at 397.3 eV corresponded to the imine (=N– bond) structure.[33] As a result, only the PPy-DBS-1 electrode exhibited a partially positively charged nitrogen structure on the surface, whereas the PPy-SS-1 and PPy-HBS-1

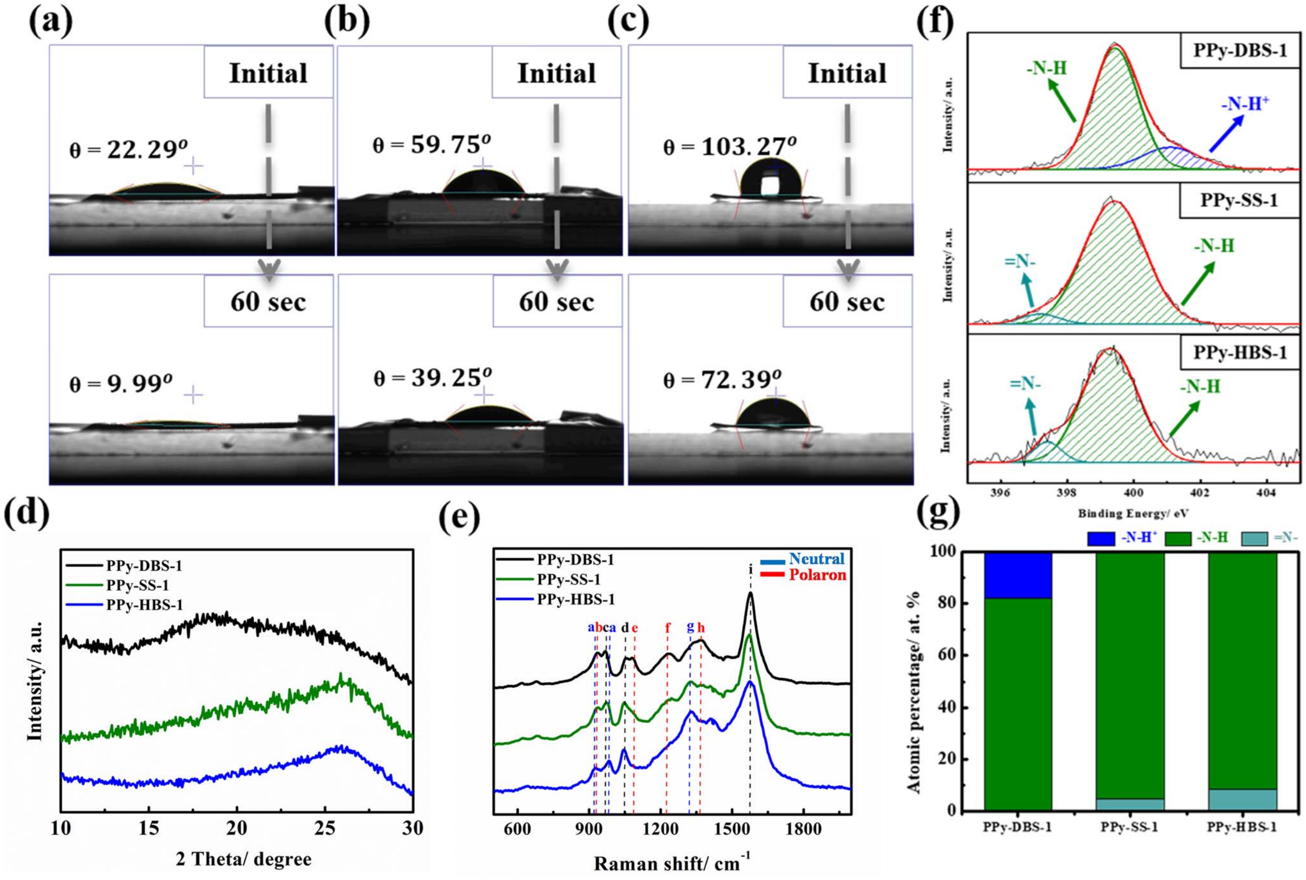

Fig. 1 Images of the water-contact angle of (a) PPy-DBS-1, (b) PPy-SS-1, and (c) PPy-HBS-1 electrodes at the same S/N molar ratio in the coating electrolyte, which depict the initial state as well as the state after 60 s using NaCl solution (10 mM). (d) XRD patterns, (e) Raman spectra, (f) XPS N 1s core level spectra, and (g) the atomic percentage of three N species for PPy-based electrodes prepared from coating electrolytes with the same S/N molar ratio.

electrodes consisted entirely of typical –N–H and =N– bonds in the neutral pyrrole ring. The atomic percentage of different N species is collated in Fig. 1g, with the PPy-DBS-1 electrode displaying the highest average oxidation state and the PPy-HBS-1 electrode demonstrating the lowest average oxidation state. Taken together, the results stated above indicated the significant influence of dopants with varying doping efficiencies on the average oxidation state of the PPy chain. These findings aligned well with the results obtained from elemental analysis and Raman spectroscopy. They also supported the notion that the size of dopants and differences in the doping efficiency greatly influenced the average oxidation state of the PPy backbone.

Besides, the partial charges in benzenesulfonate analogues were estimated *via* the density functional theory (DFT) at the B3LYP/6-31G* level of theory using Gaussian 16 (Fig. S5†). The similar levels observed on sulfonic acid suggested that the main factors affecting the average oxidation state of the PPy backbone were the alteration of the *para*-substituted groups on benzenesulfonate analogues and difference in the doping efficiency. In particular, the PPy-DBS-1 electrode showed a higher average oxidation state, indicating more favorable charge-carrier mobility. Therefore, we verified this idea through electrochemical impedance spectroscopy (EIS) (Fig. S6†), where the diameter of the semicircle determines the charge-transfer resistance (R_{ct}).[34] The PPy-DBS-1 electrode had a lower R_{ct} compared with that of PPy-SS-1 and PPy-HBS-1 electrodes, which was consistent with their respective average oxidation states. This phenomenon indicates that a higher average oxidation state enhances the charge-carrier mobility in the PPy skeleton, resulting in improved conductivity and low impedance to charge transfer of the electrode which, ultimately, reduces energy consumption in the ECDI system.

3.1.2. PPy electrodes with three dopants with the same actual S/N ratio. To gain an intuitively deep understanding of host–dopant interactions on the PPy chain, it was imperative to precisely modulate the actual S/N ratio by controlling the dopant concentration in the coating electrolyte. Fig. 2a–c presents the results of the elemental analysis with a random sampling of the controlled S/N molar ratio at 0.4–0.9 in the coating electrolyte. The actual S/N ratio of dopants could be regulated within a specific range of dopant concentration using a calibration curve. Notably, despite its relatively large molecular size, DBS exhibited a desirable doping behavior evidenced by a linear calibration curve with a slope close to 1 (Fig. 2a). Conversely, HBS displayed the lowest doping ability among the

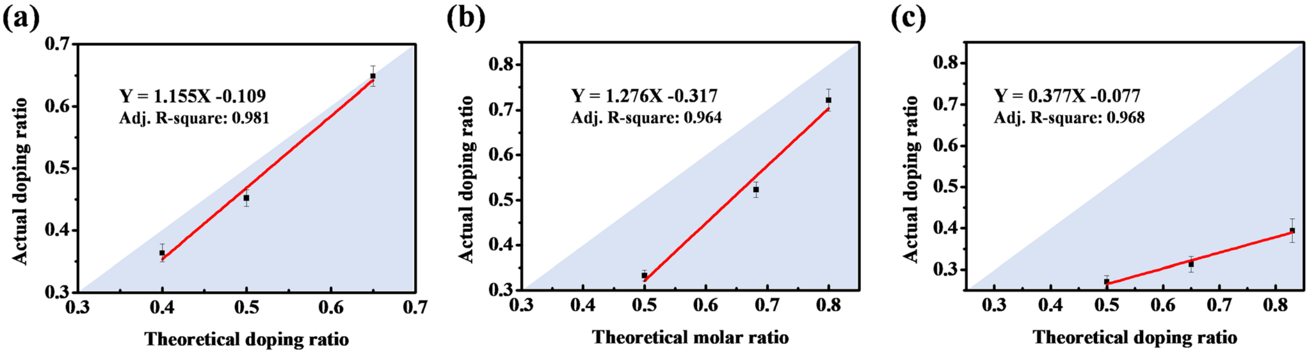

Fig. 2 Calibration curves between the S/N molar ratio in the coating electrolyte and actual S/N doping ratio in PPy for (a) PPy-DBS, (b) PPy-SS, and (c) PPy-HBS electrodes.

three dopants, probably due to its smallest molecular size (Fig. 2c). These findings highlighted the molecular size of dopants to be the primary factor affecting the doping ability in the PPy chain.

By utilizing the calibration curve in Fig. 2, we employed electrochemical polymerization to prepare PPy-SS-2 and PPy-HBS-2 electrodes, and maintained an identical S/N molar ratio to that of the PPy-DBS-1 electrode (actual S/N doping ratio = 0.45). The hydrophilicity of PPy-SS-2 and PPy-HBS-2 electrodes was improved significantly, as evidenced by the contact-angle images (Fig. 3a and b), which could be attributed to the increased density of the hydrophilic functional group in the electrodes. The difference in hydrophilicity among the three electrodes (including PPy-DBS-1) could be derived from the ability of dopants to induce changes in the PPy structure. Moreover, SEM images (Fig. S7†) indicated that increasing the actual S/N ratio of SS and HBS dopants had a negligible impact on the macroscopic morphology and thickness of the resultant PPy electrodes, which suggested that the size of these dopants was insufficient to alter PPy morphology significantly. On the other hand, XRD analysis was utilized under the same actual S/N ratio to elucidate the microstructure of PPy electrodes (Fig. 3c). Upon increasing the dopant ratio in PPy-SS-2, a secondary peak emerged alongside the original broad peak (located at approximately $2\theta = 20°$), indicating that the SS dopant may induce a similar microstructure to that of the PPy-DBS-1 electrode at a suitable doping level. However, due to the limited length of the carbon chain in the SS dopant, smaller SS micelles extended the *d*-spacing of the PPy chain only partially to 4.439 Å. Also, and the reduced signal intensity suggested that this relaxed structure may exist only partially within the PPy electrode. Besides, the peak intensity at around $2\theta = 26°$ was higher for the PPy-HBS-2 electrode than for the PPy-HBS-1 electrode. This phenomenon suggested that enhancement of the S/N molar ratio could promote the short-range ordering of the PPy chain for benzenesulfonate analogues with hydroxyl groups in the *para*-position.

Furthermore, Fig. S8† was used to examine the effects of increased doping levels on the CV curves of PPy-SS and PPy-HBS electrodes. For the PPy-SS-2 electrode, the redox pair at positive potentials remained relatively stable, but a marked increase in response currents for the redox pairs at negative potentials was discernible, along with an expanded potential range. These data suggested an enhancement in the doping efficiency bolstered

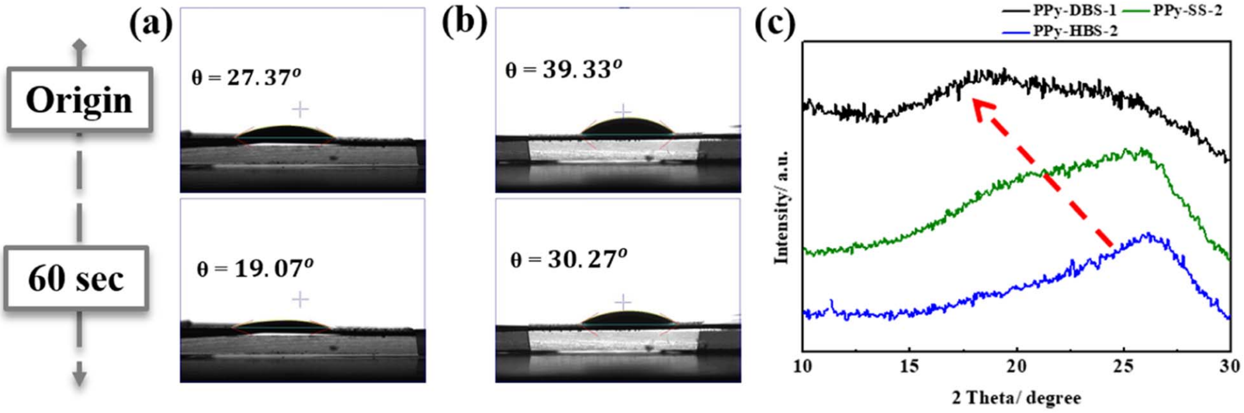

Fig. 3 Images for the water-contact angle of (a) PPy-SS-2 and (b) PPy-HBS-2 electrodes at the same actual S/N ratio of 0.45, which depict the initial state as well as the state after 60 s using NaCl solution (10 mM). (c) XRD patterns of PPy-based electrodes with the same actual S/N doping ratio.

the cation-exchange efficiency. This finding could be ascribed to the high doping level making the PPy-SS-2 electrode exhibit structural characteristics similar to those of the PPy-DBS-1 electrode (refer to Fig. 3c), thereby improving the cation-exchange capability. Conversely, an increase in the doping level of the PPy-HBS-2 electrode showed a tendency towards anion exchange, suggesting that the PPy-HBS-2 electrode may be unstable during ECDI.

The results for XPS at the N 1s core level, Raman spectroscopy, and EIS are presented in Fig. 4a–c to further investigate host–dopant interactions in PPy electrodes with three dopants at the same actual S/N ratio. In Fig. 4a, XPS at the N 1s core level unveiled the coexistence of –N–H and –N–H$^+$ peaks on the PPy chain surface across the three electrodes. The presence of partially positively charged nitrogen structures implied a high average oxidation state for all electrodes. Furthermore, the peaks centered at 1084, 1227, and 1377 cm^{-1} in the Raman spectra in Fig. 4b indicated the presence of protonated polarons in the polymer chains doped with all three dopants when the actual S/N ratio reached 0.45, which was consistent with the results of XPS at the N 1s core level. In addition, the negative Nyquist plot of EIS results (Fig. 4c) demonstrated that PPy electrodes with different dopants exhibited similar R_{ct} at the same actual S/N ratio. This phenomenon underscored the pivotal role of protonated polarons in augmenting charge-carrier mobility within the PPy framework and its strong correlation with the actual dopant ratio. Beyond a critical threshold of doping, charge-carrier pairs emerge to enable charge transfer through the electron–hole pairs facilitated by the main chain of PPy. The distinct slopes (PPy-DBS-1 > PPy-SS-2 > PPy-HBS-2) observed in the low-frequency region provided evidence of varying the capabilities of sodium-ion diffusion in active materials.[35] Notably, PPy-DBS-1 and PPy-HBS-2 electrodes demonstrated the highest and lowest ion-transfer capability, respectively. Considering the impact of dopants on the *d*-spacing of PPy-based electrodes, the dopant-induced relaxed agglomerative structure in the PPy chain was believed to affect the ion-transfer capability, potentially improving the ion-removing/-concentrating performances of the resultant ECDI system.[36,37]

3.2. Desalination performance of PPy-based ECDI systems

The desalination performances of PPy-based systems were examined using a flow-by ECDI cell (Fig. S1†). According to our

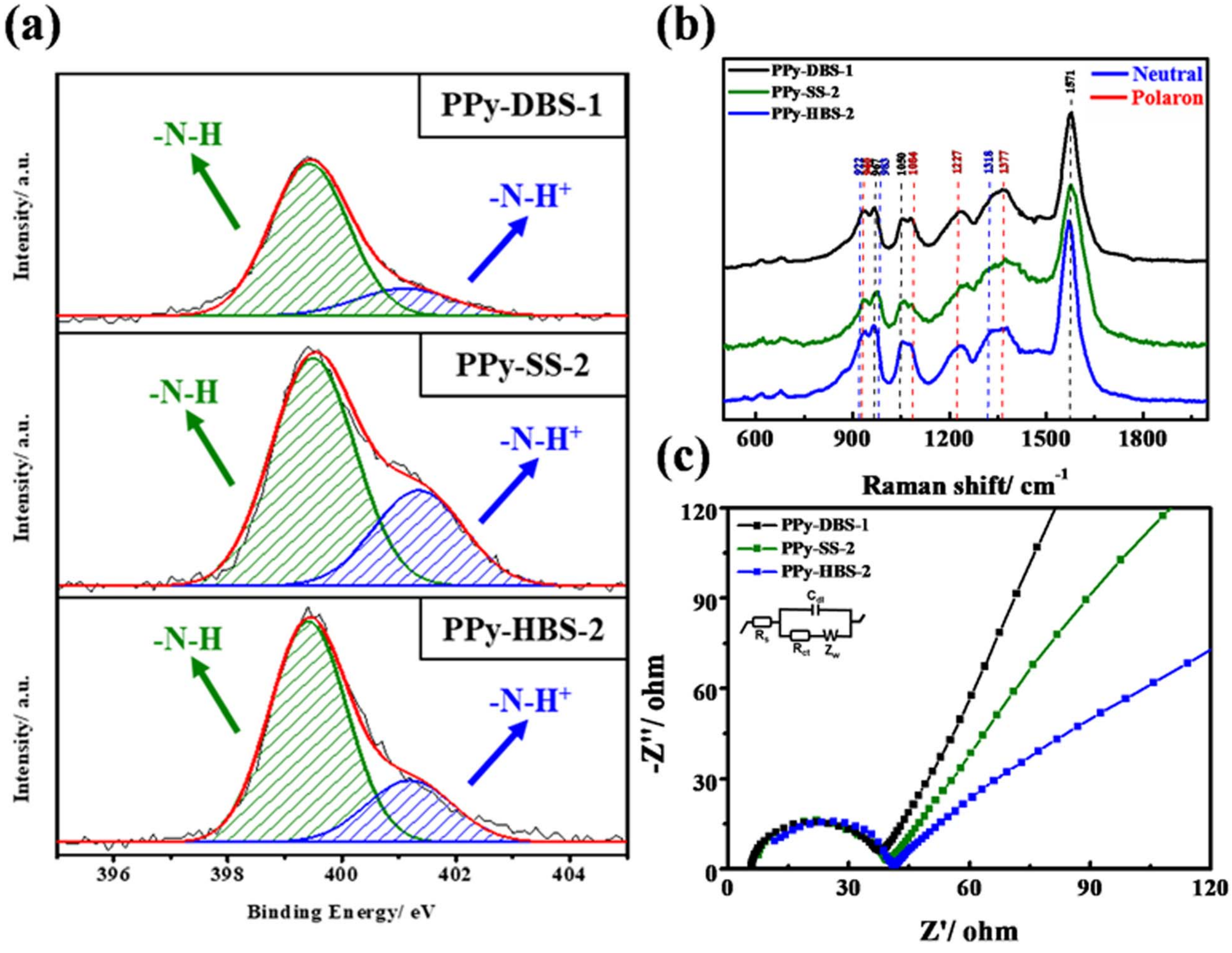

Fig. 4 (a) XPS N 1s core level spectra, (b) Raman spectra, and (c) negative Nyquist plot of PPy-DBS-1, PPy-SS-2, and PPy-HBS-2 electrodes with the same actual S/N ratio of 0.45. EIS data were measured in NaCl (10 mM) under their open-circuit potentials (E_{OCP}).

previous work, a PPy-ClO_4 electrode was used as the negative electrode for the ECDI system. This was due to the acknowledged efficacy of the ClO_4^- dopant in boosting the chloride-removal capability.[38] For the positive electrode, the doping ions within PPy films were varied so that we could ascertain their influence on effective utilization of active materials. The specifics of the ECDI process, including the removal and release of anions and cations through charge transfer during charging–discharging cycles, are depicted in Fig. S9.† In addition, to control mass loading on positive and negative electrodes through electropolymerization in the ECDI system, calibration curves of charge *versus* mass loading of PPy electrodes with various dopants were created (Fig. S10†).

Herein, a voltage-programming method was employed to confirm the optimal operation parameters for various PPy-based ECDI systems to achieve the maximum saturated SAC (Fig. 5a–c). Fig. 5a reveals that, with a random sampling of various mass loading ratios (PPy-DBS-1//PPy-ClO_4: 1.15, 1.4, 1.7, and 2.5) while maintaining a charge cell voltage of 0.8 V, the SAC was improved significantly at an optimal mass loading ratio of 1.15. Moreover, under a discharge–voltage range between −0.7 V and −0.8 V, the long charge/discharge time (60 min/60 min) test yielded a maximum SAC of ~90 mg g^{-1}. Upon replacing the positive electrode with PPy-SS-1, the optimal discharge voltage and mass loading ratio could be evaluated from Fig. 5b. The highest SAC was achieved with a mass loading ratio of 1.2 among various ratios (PPy-SS-1//PPy-ClO_4: 1, 1.2, 1.4, 1.6). In addition, when the mass loading ratio was fixed at 1.2, this system exhibited the maximum SAC (~75 mg g^{-1}) at a discharge voltage between −0.6 V and −0.8 V. Notably, −0.6 V was identified to be the optimal discharge voltage because it could enhance the SAC at a relatively low cell voltage. Fig. 5c presents the SAC profiles of the PPy-HBS-1//PPy-ClO_4 system with various mass loading ratios (PPy-HBS-1//PPy-ClO_4: 0.9, 1.05, 1.2, and 1.5) while maintaining the charge voltage at 0.8 V. The optimized discharge voltage and mass loading ratio should be −0.6 V and 1.05, respectively, because these parameters enhanced the desalination performance of the PPy-HBS-1//PPy-ClO_4 system effectively.

Fig. S11† presents the specific SAR values for three PPy-based ECDI systems during the long-time discharge processes. The PPy-DBS-1 system possessed the highest average SAR and the slowest decay rate in specific SAR. This phenomenon was attributable to the micelle formation induced by the DBS dopant, which generated a "loose" PPy structure. This increased *d*-spacing enhanced the transportation of hydrated and partially hydrated sodium ions, leading to a superior desalination rate and PPy utilization. Notably, the specific SAR of the systems using PPy-SS-1 and PPy-HBS-1 displayed similar trends. The system with PPy-SS-1 exhibited a higher average SAR in the long-term operation due to the difference in doping efficiency of the respective dopant ions at the same molar ratio. All systems provided relatively high SAR in the discharge step at discharge time ≤30 min. Hence, the optimal desalination discharge time was 30 min, and the salt adsorption and desorption could be balanced by a 20 min charge time in each cycle.

According to our previous work, fine-tuning the mass loading of PPy-based electrodes demonstrated the potential to

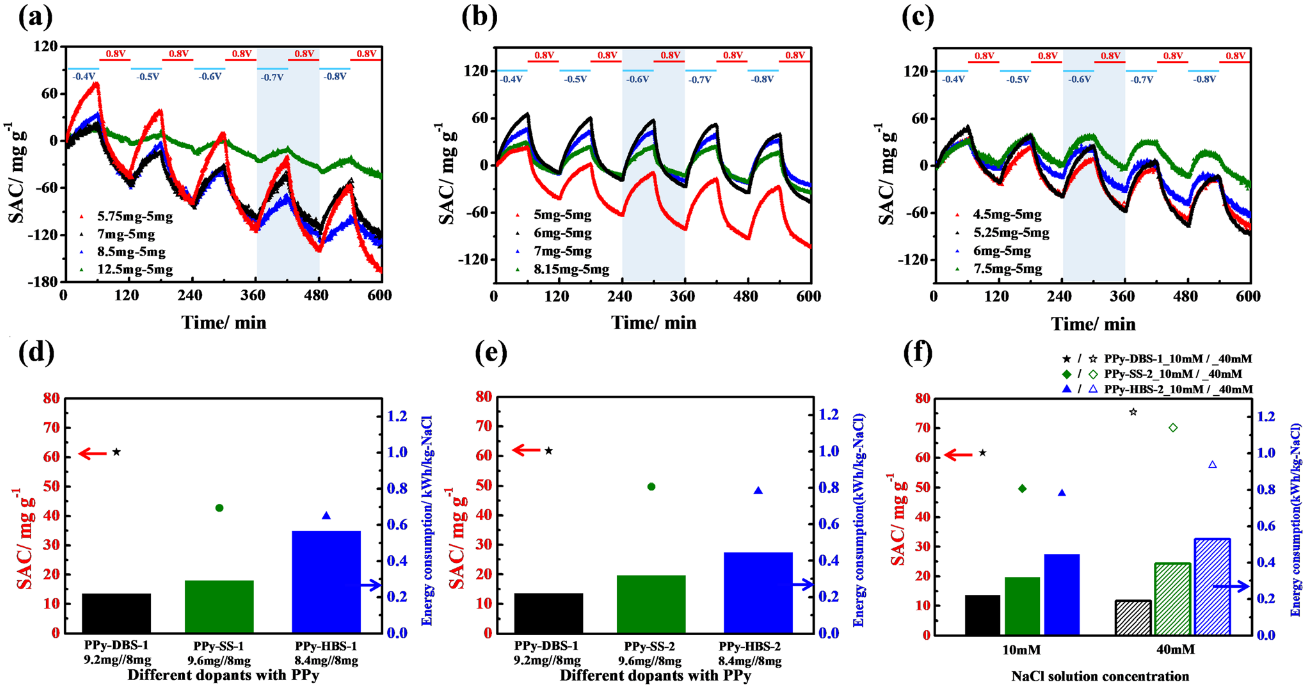

Fig. 5 Profiles for salt removal-release in NaCl (10 mM) for (a) PPy-DBS-1//PPy-ClO_4, (b) PPy-SS-1//PPy-ClO_4, and (c) PPy-HBS-1//PPy-ClO_4 cells with various mass loading ratios. The charge voltage was fixed at 0.8 V. The discharge voltage ranged from −0.4 V to −0.8 V. Plot of SAC and energy consumption for the above three ECDI cells under fixed operating parameters, where (d) PPy was prepared from the coating electrolyte with the same S/N molar ratio, (e) PPy with the same actual S/N ratio, and (f) PPy with the same actual S/N ratio in NaCl solutions (10 and 40 mM).

augment the desalination capacity of ECDI systems.[19] Fig. S12† and 5d illustrate the SAC and EC values across three PPy-based ECDI systems with regard to alterations in the mass loading of active materials. Under a consistent mass loading ratio, appropriate evaluation of the mass loading of negative electrodes (from 5 mg to 8 mg) could bolster the SAC and EC performances of PPy-based ECDI systems. In addition, the PPy-DBS-1//PPy-ClO_4 system in Fig. 5d achieved the highest SAC (61.7 mg g^{-1}) and still maintained a low EC of 0.22 kW h/kg-NaCl. This superior performance was attributable to the hydrophilic, relaxed agglomerative structure of the PPy-DBS-1 electrode and high proportion of polaron formation, which enhanced the utilization, ion-transfer capability, and charge-carrier mobility of the resultant PPy. Despite the appropriate increase in the electrode mass load to mitigate the impact of doping efficiency on SAC, the system using PPy-HBS-1 needed a relatively high energy consumption (~0.4 kW h/kg-NaCl). This could be attributed to the differences in the hydrophilicity of PPy chains and doping efficiency, leading to increased energy consumption for ion removal.

Fig. 5e compares the SAC and EC for three PPy-based ECDI systems under the same actual S/N ratio to assess if the desalination performance is independent of the doping efficiency and hydrophilicity. The PPy-DBS-1 system continued to be superior in SAC and EC due to its relaxed agglomerative PPy chain structure induced by DBS micelles. This structure facilitated the movement of hydrated and/or bare sodium ions within the electrode to access the most active sites within the PPy framework and eventually achieve excellent desalination performance. Besides, the similar SAC performance of PPy-SS-2 and PPy-HBS-2 systems in NaCl solution (10 mM) suggested that the doping efficiency critically affected the SAC during material design. Despite the comparable average oxidation states, conductivity, and hydrophilicity of PPy-SS-2 and PPy-HBS-2 electrodes, notable differences in the EC performance were observed. Hence, the difference in dopant-induced PPy structures was believed to influence the EC performance. In the PPy-SS-2 system, the relatively large *d*-spacing (4.439 Å) induced by the relatively small SS micelles could provide certain pathways for the movement of partially hydrated/bare sodium ions, potentially leading to reduced EC. Conversely, the PPy-HBS-2 electrode, in which the size of the HBS dopant was insufficient to affect the aggregation of PPy chains, hardly removed partially hydrated/bare sodium ions, thereby necessitating high energy consumption for ion removal.

To further explore the influence of dopant-induced aggregation of PPy chains on the removal of hydrated cations, long-term desalination experiments were conducted on the PPy-DBS-1 and PPy-HBS-2 systems in solutions of LiCl, NaCl, and KCl at 10 mM (Fig. S13†). The PPy-DBS-1 electrode seemed to offer more pathways for the movement of hydrated/partially hydrated cations. This phenomenon was believed to subsequently create the cation-accessible active sites and promote PPy utilization, thereby upholding the efficacy of monovalent cation removal even upon adjustments to the charge/discharge time. Conversely, the PPy-HBS-2 system exhibited a constrained efficacy of lithium-ion removal, particularly apparent if the discharge time >20 min. This observation implied a potential scarcity of effective pathways for the free movement of hydrated/partially hydrated cations, leading to relatively poor utilization of active sites. Consequently, this circumstance reduced the cation-removal capacity of the PPy-HBS-2 system significantly.

To investigate the influence of varying salt concentrations on the desalination performance of three ECDI cells, two types of NaCl solutions (10 mM and 40 mM) were used to examine the SAC and EC of PPy-DBS-1, PPy-SS-2, and PPy-HBS-2 systems (Fig. 5f). Results revealed noteworthy enhancements in SAC for the two cells using PPy-DBS-1 and PPy-SS-2 electrodes in NaCl solution (40 mM), respectively, culminating in ~75 mg g^{-1} and 70 mg g^{-1} during a 30 min discharge step. Intriguingly, these SAC levels bore parity with the performance exhibited by both cells in the 10 mM NaCl solution during a 60 min discharge step. This concordance suggested that these cells had effective desalination capabilities, particularly in a relatively concentrated environment, due to their efficient utilization of active sites. Furthermore, stemming from the improvement in SAC, observation of a similar EC performance in the salt media at two concentrations implied that the presence of loosely agglomerative PPy chains could enhance the efficiency of desalination.

Through the integration of material analyses and deionization tests, predictive models for the impact of dopants on the desalination mechanism of the PPy chain during salt removal could be created (Fig. 6), which may apply to other conducting polymers. The surfactant-like DBS molecule enabled the formation of micelle structures,[27] thereby inducing a relaxed agglomerative structure of the PPy-DBS-1 electrode (Fig. 6a).[39] In addition, XRD analysis revealed that the *d*-spacing (4.92 Å) of PPy chains in the PPy-DBS-1 electrode was larger than the radius of hydrated sodium ions (3.58 Å).[40] This feature facilitated the entry of hydrated and bare sodium ions into the PPy chain, thereby amplifying utilization of active sites. The surfactant also could enhance the hydrophilicity of the PPy-DBS-1 electrode, promoting ion transport between the electrode and solution. Therefore, the PPy-DBS-1 system exhibited the optimal SAC performance with the same actual S/N ratio in a short-term cycling test.

Fig. 6b shows that the micelle structure of the SS dopant was smaller than that of the DBS dopant due to the shorter chain length. This hypothesis was supported by the peak shift of the pyrrole–anion interaction in XRD patterns at around $2\theta = 20°$ (*d*-spacing = 4.43 Å) indicating that, compared with DBS, the SS dopant has a less pronounced ability to induce the relaxed agglomerative structure in PPy chains. Therefore, based on the significant impacts of discharge times (30 min/60 min) and solution concentrations (10 mM/40 mM) on the desalination performance, the PPy-SS-2 film was believed to provide only a partially relaxed agglomerative structure and could only utilize certain pathways to remove hydrated sodium ions during desalination, consequently impeding complete utilization of active sites. This limitation restricted the desalination performance of this PPy system at low NaCl concentrations and short operating times. However, under a sufficiently high doping level induced by the SS dopant, the PPy electrode could use similar pathways for the transfer of hydrated and bare sodium ions to

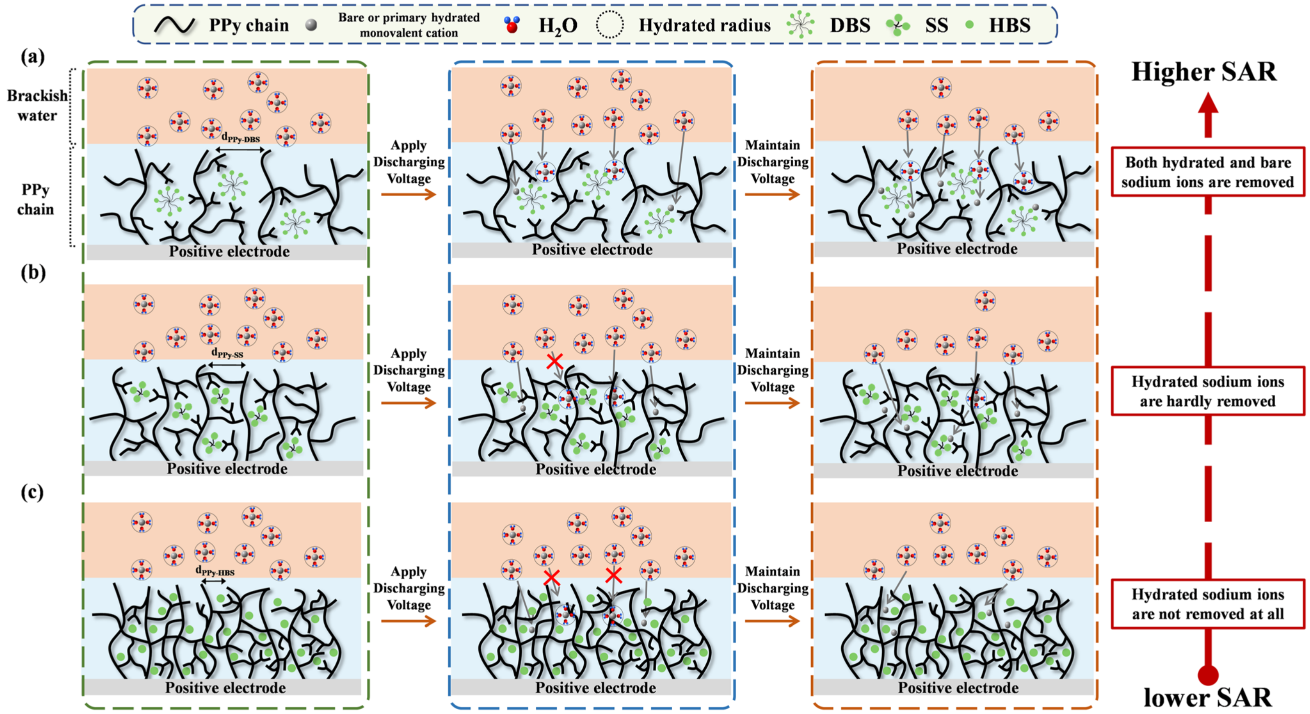

Fig. 6 Mechanism of the electrochemical deionization of PPy chains doped with (a) DBS, (b) SS, and (c) HBS (schematic).

active sites, leading to a significantly improved SAC performance in response to the higher salt concentration or longer desalination time.

In contrast, the scheme in Fig. 6c indicates that the HBS dopant size was insufficient to induce the relaxed agglomeration of the PPy chains. This limitation hindered the generation of effective pathways for hydrated-cation movement within the electrode, resulting in poor utilization of active sites. Furthermore, as the operation time increased, most of the active sites for bare-cation adsorption were occupied, resulting in a significant decline in the cation-removal performance and fastest decay in the specific SAR for the cell using the PPy-HBS-2 electrode. This structural constraint sacrificed the cation-removal capability but also increased the energy consumption required for ion removal. Therefore, DBS appeared to be the most suitable dopant for promoting the relaxed agglomeration of PPy chains and enhancing the cation-removal capability of PPy-based positive electrodes in ECDI systems.

3.3. PPy-DBS//PPy-ClO_4 system at various doping ratios

The DBS dopant was beneficial for enhancing the cation-capturing ability of the PPy-based electrode, so we further investigated the optimal doping ratio of this PPy film. Using the calibration curve from Fig. 2a, we prepared the PPy-DBS-2 electrode with a S/N doping ratio = 0.4 and PPy-DBS-3 electrode with a S/N doping ratio = 0.65. Data from SEM and contact-angle images of PPy-DBS-2 and PPy-DBS-3 electrodes are presented in Fig. 7 and S14.† Variations in the doping ratio of PPy-DBS electrodes led to notable changes in the surface morphology of PPy electrodes because PPy with a higher doping ratio showed a more pronounced feature. A similar trend was observed in contact-angle measurements, whereby higher doping ratios corresponded to better hydrophilicity and *vice versa*. XRD analysis (Fig. S15†) illustrated slight enhancement in ordering of the relaxed agglomerative structure induced by the DBS dopant on PPy chains upon increasing the doping ratio from 0.4 to 0.65.

CV (Fig. S16†) was used to explore how variations in doping levels for PPy-DBS electrodes affect their ion-exchange characteristics. At a low doping level (refer to the PPy-DBS-2 electrode), CV curves predominantly exhibited cation-exchange behavior, with the efficiency of cation exchange improving concomitantly with the increased doping level (refer to the PPy-DBS-1 electrode). However, upon further increase in the doping level, a second redox pair emerged in the corresponding CV curve (refer to the PPy-DBS-3 electrode). This observation suggested that excessively high doping ratios led to a “too relaxed” structure which, in turn, heightened the efficiency of anion exchange. In addition, Raman spectroscopy and XPS analysis (Fig. S17†) showed that PPy-DBS electrodes with all doping ratios exhibit the bonds of –N–H and $–N–H^+$ structures on the surface of PPy chains, indicating the formation of protonated polarons. Moreover, the increase in the average oxidation state observed in the previous experiment reduced the charge-transfer impedance of the active material. These findings suggested that control of the DBS doping level had a greater influence on hydrophilicity and active sites compared with the induction of a more relaxed agglomeration of PPy chains.

In addition, the desalination performance of ECDI cells using PPy electrodes in various DBS doping ratios was

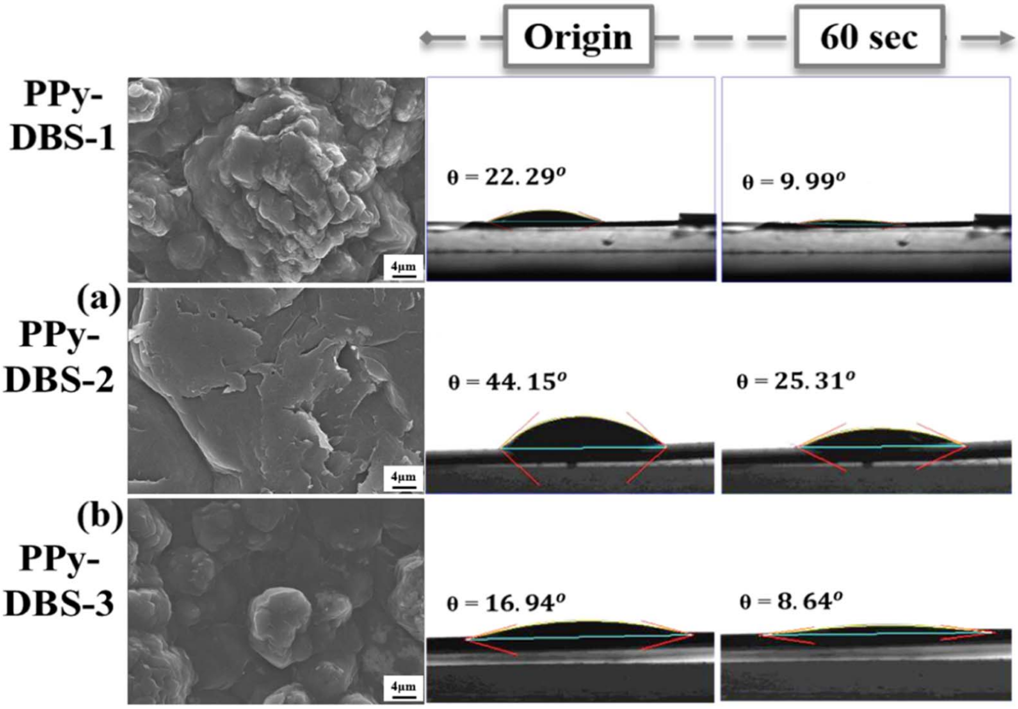

Fig. 7 Images of low-magnification SEM and water-contact angle of (a) PPy-DBS-2 and (b) PPy-DBS-3 electrodes at S/N ratios of 0.4 and 0.65, respectively. Images of water-contact angle include the initial state after 60 s using NaCl solution (10 mM). Results of PPs-DBS-1 at the S/N ratio of 0.45 are shown for comparison.

undertaken. Fig. 8a visualizes the order of electrodes with respect to decreasing SAC for a fixed charge/discharge time of 20 min/30 min: PPy-DBS-3 > PPy-DBS-1 > PPy-DBS-2. This trend corresponded to the variation of DBS doping ratios, thereby highlighting the strong correlation between SAC and the actual doping ratio. Furthermore, the difference in EC among the three cells stated above was negligible, suggesting that the degree of protonation had a greater influence on the desalination performance compared with the doping ratio.

To assess cycling stability, long-term cycling tests were conducted on PPy-DBS//PPy-ClO_4 systems with varying doping ratios. Fig. 8b presents the results for a charge/discharge time of 20 min/30 min per cycle over a total cycling time of 41.7 h (50 cycles). The PPy-DBS-3//PPy-ClO_4 system initially exhibited the highest SAC ($\sim$70 mg g^{-1}) in the first 10 cycles, but the R_{SAC} experienced a significant decline to only 46% in the final cycle. In contrast, the PPy-DBS-1//PPy-ClO_4 system showed a comparable initial SAC ($\sim$65 mg g^{-1}) and maintained the R_{SAC} of 83% after 50 cycles, indicating a favorable SAC performance and sustained stability.

Compared with other high-stability ECDI systems reported in the literature,[6,15,16,19,37,41–45] Fig. 8c and Table S4† showed that our PPy-DBS-1//PPy-ClO_4 system achieved the highest SAC performance with an acceptable cycle life. Moreover, the XRD patterns in Fig. S18† showed varying degrees of attenuation in the characteristic peaks of PPy-based positive electrodes after a long cycling test, particularly in the case of PPy-DBS-3. In addition, SEM images at various magnifications and cross-sectional views were used to evaluate the morphologic changes in PPy-DBS electrodes following multiple desalination cycles. Fig. S19† indicated that repeated cycling tests did not alter the surface and cross-sectional morphology of the PPy-DBS-1 electrode significantly. In contrast, structural collapse and change in surface morphology in the PPy-DBS-3 electrode were found (Fig. S20†). The bulk structure present originally on the surface disappeared and was replaced with numerous cracks, as confirmed through high-magnification and cross-sectional SEM images. This phenomenon suggested that an overly loose structure could render anion exchange involving the DBS dopant. It also suggested that the exchange of large anions ultimately resulted in structural collapse of the PPy-DBS-3 electrode, resulting in fewer active sites available for deionization. Therefore, we concluded that, while a relaxed agglomerative structure of the PPy chain could achieve a high SAC and SAR, this could compromise the sustainability of the ECDI system. Hence, efforts should be made to maintain the structural integrity of the conducting polymer to ensure the overall performance of the ECDI system.

We wished to validate the synergistic effect of dopants and the PPy chain in promoting PPy-based electrodes for ECDI systems. A plot was constructed using SAC and EC as the crucial metrics to juxtapose the outcome of our work and that for other high-efficient ECDI systems reported over the past 3 years[6,15,16,19,37,41–43,46–50] (refer to Table S5†). Remarkably, among the systems examined in this work, the PPy-DBS-1//PPy-ClO_4 system demonstrated a desirable trade-off between performance and sustainability. As presented in Fig. 8d, this system exhibited significantly lower EC levels compared with those of

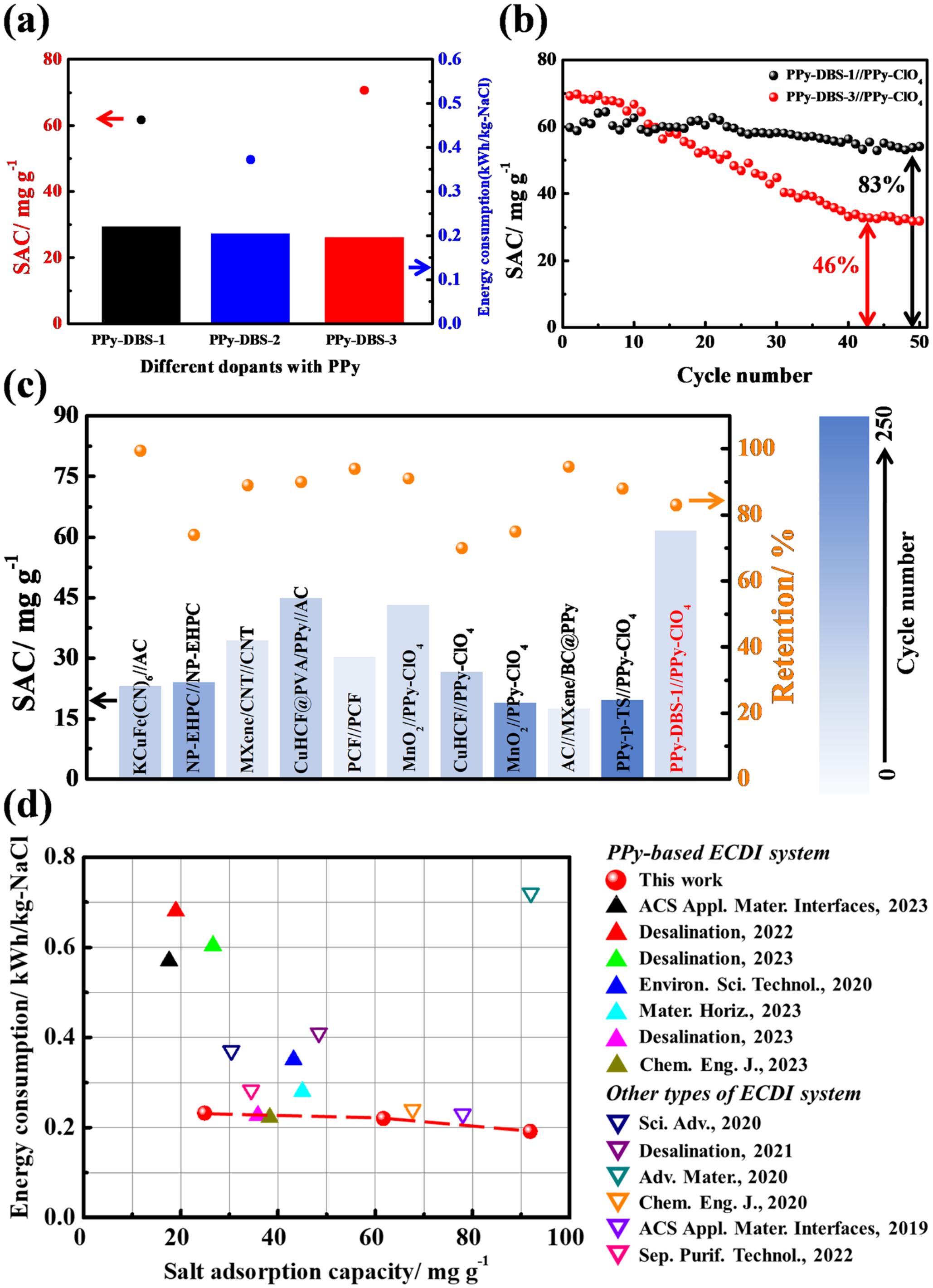

Fig. 8 (a) SAC and EC performances and (b) specific SAC *vs.* cycle number for cells using positive electrodes with various DBS doping ratios. Cells with mass loading of 8 mg on PPy-ClO_4 electrodes were charged/discharged at constant voltages (0.8 V/−0.7 V) in NaCl solution (10 mM). (c) Comparisons of cycling stability among various ECDIs in terms of SAC, SAC retention, and cycle number (bars represent the cycle number, with darker colors denoting more cycles). (d) EC-SAC plot for comparisons of other ECDI systems in the literature (data include this work, conducting polymer-based ECDIs, and other types of ECDI systems).

alternative ECDI systems and showcased the proficient SAC in brackish water simultaneously. This improved performance could be attributed to the specific dopant species, such as DBS, facilitating the formation of an ion-transport pathway and enhancing the charge-carrier mobility within the PPy framework, thereby leading to the high utilization of PPy. These discoveries underscore the remarkable potential of dopant synergies in promoting the utilization of conducting polymers within ECDI systems and ion-trapping applications.

4. Conclusions

We provided valuable insights into the synergistic relationship between dopants and the PPy chain, a field that lacks comprehensive understanding in desalination research. First, the SAC performance was highly dependent upon the doping efficiency of PPy, which could be built by *para*-substituted groups and according to the concentration of dopants in the coating electrolyte. Meanwhile, high hydrophilicity and the presence of protonated polarons on the PPy chain could enhance ion transport and the mobility of charge carriers within the PPy film, effectively promoting the utilization of conducting polymers and reducing the energy consumption of the ECDI system. At the same actual S/N ratio, dopants with long carbon chains in *para*-substituted groups (*e.g.*, DBS and SS) tended to form micelles. This phenomenon resulted in a large *d*-spacing that facilitated the migration of sodium ions and augmented the efficiency of active sites formed by dopants, as reflected in low EC and large maximum SAC at low NaCl concentrations. Notably, increasing the PPy-DBS doping ratio could enhance the ability of the electrodes to capture cations (though this could negatively impact the cycling stability of the ECDI system). Overall, our findings elicited important insights into the role of dopants in constructing agglomerative PPy chains for cation removal. They also provide guidelines for engineering the PPy microstructure to optimize the performance but maintain the cycling stability in PPy//PPy-based ECDI systems.

Author contributions

Hung-Yi Huang: conceptualization, methodology, validation, data analysis, investigation, data curation, writing (original-draft preparation, review and editing), and data visualization. Yi-Heng Tu: conceptualization, methodology, validation, investigation, and writing (original-draft preparation, review and editing). Yu-Hsiang Yang: methodology and validation. Yi-An Chen: methodology, investigation, and writing (review and editing). Wei-Lin Lee: curation and visualization of data. Meng-Fei Wu: curation and visualization of data. Ho-Hsiu Chou: methodology, data analysis, and resources. Chi-Chang Hu: conceptualization, methodology, validation, data analysis, investigation, resources, writing (original-draft preparation, review and editing), data visualization, supervision, project administration.

Conflicts of interest

There are no conflicts of interest to declare.

Acknowledgements

Financial support of this work, by the National Science and Technology Council of Taiwan (NSTC 112-2221-E-007-021-MY3), is gratefully acknowledged.

References

1 M. T. Van Vliet, E. R. Jones, M. Flörke, W. H. Franssen, N. Hanasaki, Y. Wada and J. R. Yearsley, *Environ. Res. Lett.*, 2021, **16**, 024020.

2 Y. Liu, K. Wang, X. Xu, K. Eid, A. M. Abdullah, L. Pan and Y. Yamauchi, *ACS Nano*, 2021, **15**, 13924–13942.

3 C.-C. Hsu, Y.-H. Tu, Y.-H. Yang, J.-A. Wang and C.-C. Hu, *Desalination*, 2020, **481**, 114362.

4 C.-W. Tai, W.-Y. Jao, L.-C. Tseng, P.-C. Wang, A.-P. Tu and C.-C. Hu, *J. Mater. Chem. A*, 2023, **11**, 19669–19684.

5 Y.-H. Tu, Y.-H. Yang and C.-C. Hu, *Desalination*, 2021, **498**, 114807.

6 Y.-H. Tu, Y.-C. Tai, J.-Y. Xu, Y.-H. Yang, H.-Y. Huang, J.-H. Huang and C.-C. Hu, *Desalination*, 2022, **538**, 115928.

7 Y.-H. Tu, C.-F. Liu, J.-A. Wang and C.-C. Hu, *Electrochem. Commun.*, 2019, **104**, 106486.

8 S. T. Chung, Y.-H. Tu, H.-Y. Huang, C.-C. Hu and D.-H. Tsai, *ACS Sustain. Chem. Eng.*, 2022, **10**, 15777–15790.

9 J. Du, W. Xing, J. Yu, J. Feng, L. Tang and W. Tang, *Water Res.*, 2023, **235**, 119831.

10 Y.-H. Tu, H.-Y. Huang, Y.-H. Yang, C.-Y. Lai, C.-W. Tai and C.-C. Hu, *ACS Appl. Mater. Interfaces*, 2023, **15**(40), 46812–46828.

11 F. Yu, L. Wang, Y. Wang, X. Shen, Y. Cheng and J. Ma, *J. Mater. Chem. A*, 2019, **7**, 15999–16027.

12 Y.-A. Chen, S.-J. Chen, L.-Y. Lee, R.-H. Lai, C.-M. Yeh, C.-A. Chiu, J.-Y. Lai, Y.-C. Lai and H.-H. Chou, *Nano Energy*, 2023, **117**, 108882.

13 Y. Cai, Y. Wang, X. Han, L. Zhang, S. Xu and J. Wang, *J. Electroanal. Chem.*, 2016, **768**, 72–80.

14 R. Wang, K. Sun, Y. Zhang, C. Qian and W. Bao, *J. Mater. Chem. A*, 2022, **10**, 6414–6441.

15 W. Xu, C. Tan, A. Wang, S. Hu, L. Deng, S. Boles, K. Sun, B. Li and H. Hu, *ACS Appl. Mater. Interfaces*, 2023, **15**, 16266–16276.

16 G. Tan, S. Lu, N. Xu, D. Gao and X. Zhu, *Environ. Sci. Technol.*, 2020, **54**, 5843–5852.

17 B. Li, Q. Cao, Y. Liu, Y. Sun, X. Ma, X. Duan, C. Chen and Y. Wang, *J. Mater. Chem. A*, 2022, **10**, 24905–24914.

18 Y. Zhao, Y. Cai, Y. Wang and S. Xu, *Sep. Purif. Technol.*, 2021, **259**, 118175.

19 H.-Y. Huang, Y.-H. Tu, Y.-H. Yang, Y.-T. Lu and C.-C. Hu, *Chem. Eng. J.*, 2023, 141373.

20 J. G. Martinez, T. F. Otero and E. W. Jager, *Langmuir*, 2014, **30**, 3894–3904.

21 M. S. Ting, B. N. Narasimhan, J. Travas-Sejdic and J. Malmström, *Sens. Actuators, B*, 2021, **343**, 130167.

22 L. Bay, N. Mogensen, S. Skaarup, P. Sommer-Larsen, M. Jørgensen and K. West, *Macromolecules*, 2002, **35**, 9345–9351.

23 M.-K. Song, Y.-T. Kim, B.-S. Kim, J. Kim, K. Char and H.-W. Rhee, *Synth. Met.*, 2004, **141**, 315–319.

24 C.-C. Hu, C.-F. Hsieh, Y.-J. Chen and C.-F. Liu, *Desalination*, 2018, **442**, 89–98.

25 M. Yan, W. Shen, N. Li, Y. Chen, Z. Xie, M. Liu and J. Wei, *J. Membr. Sci.*, 2023, 121753.

26 M. Zhang, A. Nautiyal, H. Du, J. Li, Z. Liu, X. Zhang and R. Wang, *Electrochim. Acta*, 2020, **357**, 136877.

27 J. Hazarika and A. Kumar, *Synth. Met.*, 2013, **175**, 155–162.

28 K. Cheah, M. Forsyth and V.-T. Truong, *Synth. Met.*, 1998, **94**, 215–219.

29 V. Syritski, A. Öpik and O. Forsén, *Electrochim. Acta*, 2003, **48**, 1409–1417.

30 M. Šetka, R. Calavia, L. Vojkůvka, E. Llobet, J. Drbohlavová and S. Vallejos, *Sci. Rep.*, 2019, **9**, 1–10.

31 I. Šeděnková, O. Taboubi, M. Paúrová, J. Hromádková and M. Babič, *Synth. Met.*, 2023, **292**, 117218.

32 H. Mao, Y. Fu, H. Yang, S. Zhang, J. Liu, S. Wu, Q. Wu, T. Ma and X.-M. Song, *Chem. Eng. J.*, 2021, **425**, 131769.

33 S. Haldar, D. Rase, P. Shekhar, C. Jain, C. P. Vinod, E. Zhang, L. Shupletsov, S. Kaskel and R. Vaidhyanathan, *Adv. Energy Mater.*, 2022, **12**, 2200754.

34 W. C. Lin, C. L. Chang, C. H. Shih, W. C. Lin, Z. Yu Lai, J. W. Chang, L. Y. Ting, T. F. Huang, Y. E. Sun and H. Y. Huang, *Small*, 2023, 2302682.

35 G. M. Weng, Y. Xie, H. Wang, C. Karpovich, J. Lipton, J. Zhu, J. Kong, L. D. Pfefferle and A. D. Taylor, *Angew. Chem.*, 2019, **131**, 13865–13871.

36 B.-S. Yin, S.-W. Zhang, Q.-Q. Ren, C. Liu, K. Ke and Z.-B. Wang, *J. Mater. Chem. A*, 2017, **5**, 24942–24950.

37 Y. Ren, F. Yu, X.-G. Li, B. Yuliarto, X. Xu, Y. Yamauchi and J. Ma, *Mater. Horiz.*, 2023, **10**, 3548–3558.

38 Y. Wu, G. Alici, J. D. Madden, G. M. Spinks and G. G. Wallace, *Adv. Funct. Mater.*, 2007, **17**, 3216–3222.

39 S. Maw, E. Smela, K. Yoshida and R. Stein, *Synth. Met.*, 2005, **155**, 18–26.

40 H. Ohtaki and T. Radnai, *Chem. Rev.*, 1993, **93**, 1157–1204.

41 Y.-H. Yang, Y.-H. Tu, H.-Y. Huang and C.-C. Hu, *Desalination*, 2023, **545**, 116160.

42 T. Liu, J. Serrano, J. Elliott, X. Yang, W. Cathcart, Z. Wang, Z. He and G. Liu, *Sci. Adv.*, 2020, **6**, eaaz0906.

43 Y. Cai, L. Zhang, R. Fang, Y. Wang and J. Wang, *Sep. Purif. Technol.*, 2022, **292**, 121019.

44 H. Zhang, C. Wang, W. Zhang, M. Zhang, J. Qi, J. Qian, X. Sun, B. Yuliarto, J. Na and T. Park, *J. Mater. Chem. A*, 2021, **9**, 12807–12817.

45 S. Choi, B. Chang, S. Kim, J. Lee, J. Yoon and J. W. Choi, *Adv. Funct. Mater.*, 2018, **28**, 1802665.

46 J. Guo, Y. Wang, H. Zhang, Y. Cai and R. Fang, *Desalination*, 2023, **548**, 116305.

47 W. Shi, X. Liu, T. Deng, S. Huang, M. Ding, X. Miao, C. Zhu, Y. Zhu, W. Liu and F. Wu, *Adv. Mater.*, 2020, **32**, 1907404.

48 A. Gong, Y. Zhao, M. He, B. Liang and K. Li, *Desalination*, 2021, **505**, 114997.

49 J. Ma, Y. Cheng, L. Wang, X. Dai and F. Yu, *Chem. Eng. J.*, 2020, **384**, 123329.

50 S. Vafakhah, L. Guo, D. Sriramulu, S. Huang, M. Saeedikhani and H. Y. Yang, *ACS Appl. Mater. Interfaces*, 2019, **11**, 5989–5998.